Journal of Sound and Vibration (2000) **234**(2), 331–348
doi:10.1006/jsvi.2000.2865, available online at http://www.idealibrary.com on IDEAL®

A LUMPED MASS MODEL FOR PARAMETRIC INSTABILITY ANALYSIS OF CANTILEVER SHAFT–DISK SYSTEMS

HONG-CHENG SHEU

Energy &Resources Laboratory, Industrial Technology Research Institute, Chutung, Hsinchu 310, *Taiwan*

AND

LIEN-WEN CHEN

Department of Mechanical Engineering, National Cheng Kung University, Tainan 701, *Taiwan*

(*Received* 27 *July* 1999, *and in final form* 4 *January* 2000)

A lumped mass model is proposed to study the parametric instability of a cantilever shaft–disk system subjected to axial and follower loads, respectively. In the present study, a set of linearized stiffness influence coefficients of a longitudinally loaded cantilever shaft is derived. The mathematical model also takes into account the effect of shear deformation. Because linearized stiffness influence coefficients are used, the governing differential equations of the system become a set of coupled Mathieu–Hill equations. By the use of Bolotin's method, the equation of boundary frequencies can be obtained and is used to determine the boundaries between stable and unstable regions. As compared to the unstable regions obtained from finite element method, the present results show not only good agreement with them, but also much easier to construct the unstable regions. From the result of numerical simulations, several destabilizing factors of the rotational cantilever shaft–disk system are found.

1. INTRODUCTION

Parametric vibration refers to oscillatory motion that occurs in a structure or a mechanical system as a result of time-dependent variation of parameters such as inertia, damping, or stiffness. Although parametric vibration is regarded to be of secondary interest, it can have catastrophic effects on mechanical systems near critical regions of parametric instability. According to the sources of the time-dependent variation, parametric instabilities of interest in the field of rotating machinery can be broadly categorized as follows:

1. Parametric instability due to unsymmetrical disk, shaft, and/or bearing characteristics [1].
2. Parametric instability due to external pulsating torque [2].
3. Parametric instability due to external pulsating longitudinal loading [3, 4].

The first two categories had been thoroughly investigated during the past 50 years. Only a few investigations, however, have been devoted to the third category. Shaft–disk systems (rotors) subjected to longitudinal forces (includes axial and follower types) due to a pressure

0022-460X/00/270331 + 18 $35.00/0

difference across the rotor disks can be found in many rotating machines. For these reasons, the present paper will focus on the parametric instability of rotating shaft–disk systems due to pulsating longitudinal loadings.

The literature on the parametric instability behavior of non-rotating structural members or machine components is voluminous [5–9], but only a small amount of work relates to rotor systems. Sinha [3] used Galerkin's method to derive the equations for determining the stability conditions of a uniform viscoelastic shaft–disk system subjected to a pulsating axial load. In his work, the Dirac's impulse function and the idea of equivalence are introduced to consider the disks mounted on the shaft at different locations. Chen and Ku [4] used the finite element method to investigate the dynamic stability of a cantilever shaft–disk system subjected to time-varying axial periodic forces.

Several well-established prediction methods are available for linear analyses of rotor systems and can be divided into three major classes according to the modelling procedure. The first is the discretization method, such as the transfer matrix method [10, 11] and the finite element method [12, 13]. The second is the analytical method in which a rotor system is treated as a continuous system whose motions are described by partial differential equations [14–17]. The third is the approximate method using lumped mass model that neglects the mass distribution of the shaft [18–20]. With the recent development of computer hardware and software, the discretization method has become a popular method for analysis of transverse vibrations of rotor systems. Analytical methods often yields highly accurate and essential information on the behavior of rotor systems. However, they are often difficult to implement and closed-form solutions are not generally possible. When the mass of the shaft is small compared to that of the disks and the higher-frequency modes are less important, lumped mass models are generally suitable for the analysis of such shaft–disk systems.

In the past, investigators generally used lumped mass models to study the dynamic behaviour of rotor systems. They usually use Euler–Bernoulli beam theory that neglects the effect of shear deformation. Furthermore, to authors' knowledge, the incorporation of the longitudinal force effect in lumped mass models has not been published. The first objective of this paper is to derive the exact stiffness influence coefficients of the cantilever shafts subjected to longitudinal forces. In order to obtain a more accurate description of the dynamic behavior of shaft–disk systems, the present shaft mathematical model also takes into account the effect of shear deformation. Because the exact stiffness influence coefficients of the shafts are highly transcendental and difficult to interpret, each stiffness influence coefficient is expanded in a Taylor's series about the longitudinal force. The stiffness influence coefficients are then approximately expressed as linear functions of the longitudinal load. The resulting lumped mass model is very suitable to deal with the problems of parametric instability caused by periodic longitudinal loads. In this paper, a lumped mass model with approximate stiffness influence coefficients is employed to derive the governing equations of the cantilever shaft–disk systems subjected to periodic longitudinal forces. The boundaries between the regions of stability and instability are constructed by applying Bolotin's method under the condition of a constant rotational speed. The effects of shear deformation, gyroscopic moment, and static longitudinal loading on the regions of parametric instability are studied.

2. MATHEMATICAL FORMULATION

A uniform circular cantilever shaft of length L, with a circular disk attached at the free end, subjected to a periodic longitudinal force $p(t)$, and rotating at a constant speed Ω is

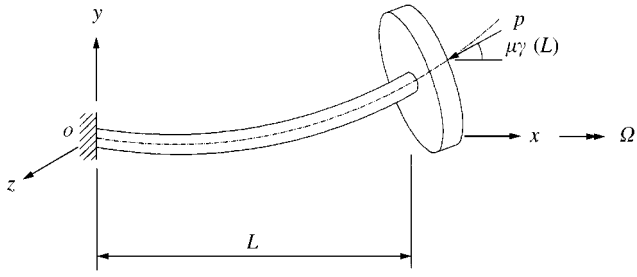

Figure 1. A cantilever shaft–disk system subjected to a longitudinal loading and its co-ordinate system.

illustrated in Figure 1. A set of inertia reference frame o-xyz, with origin o at the left end of the shaft, is adopted. The following assumptions of the present rotor system are made.

1. The mass of the shaft is neglected compared with that of the disk.
2. The axial motion of the shaft is small and can be reasonably neglected.
3. The attached disk is rigid with mass M_D, and diameteral and polar moments of inertia I_D, I_P, respectively.
4. The flexibility of the bearing is neglected compared with that of the shaft.

2.1. EQUATIONS OF MOTION

The displacement and orientation of the disk are described by the translations V and W in the y- and z- directions and small rotations B and Γ about y- and z-axis. Using a Newtonian approach, the following governing equations of the rotating cantilever shaft–disk system can be obtained [19]:

$$M_D\ddot{V} + k_{11}V + k_{12}\Gamma = 0, \tag{1}$$

$$M_D\ddot{W} + k_{11}W - k_{12}\mathrm{B} = 0, \tag{2}$$

$$I_D\ddot{B} + \Omega I_P\dot{\Gamma} - k_{21}W + k_{22}\mathrm{B} = 0, \tag{3}$$

$$I_D\ddot{\Gamma} - \Omega I_P\dot{\mathrm{B}} + k_{21}V + k_{22}\Gamma = 0, \tag{4}$$

where k_{ij}, $i, j = 1, 2$, are stiffness influence coefficients of the cantilever shaft subjected to a longitudinal force, and can be determined using mechanics of solids. The detailed procedure is shown in Appendix A.

Introducing the complex notations

$$U = V + \mathrm{j}W, \quad \Psi = \Gamma - \mathrm{j}\mathrm{B}. \tag{5, 6}$$

Equations (1)–(4) can be conveniently expressed as

$$M_D\ddot{U} + k_1U + k_{12}\Psi = 0, \tag{7}$$

$$I_D\ddot{\Psi} - \mathrm{j}\Omega I_P\dot{\Psi} + k_{21}U + k_{22}\Psi = 0. \tag{8}$$

2.2. APPROXIMATE EXPRESSIONS FOR STIFFNESS INFLUENCE COEFFICIENTS

Although the exact stiffness influence coefficients had been derived in Appendix A, they are highly transcendential and difficult to interpret. A simplified approximate expression for each k_{ij} can be obtained by expanding it in a Taylor's series about $p = 0$, i.e.

$$k_{ij} \approx k_{ij}^a + pk_{ij}^b, \tag{9}$$

where only first order terms in p have been retained and

$$k_{ij}^a = k_{ij}|_{p=0}, \quad k_{ij}^b = \left.\frac{\partial k_{ij}}{\partial p}\right|_{p=0}. \tag{10, 11}$$

The parameter p is taken as positive if the longitudinal load is compressive and as negative if it is tensile.

The factors of k_{ij}^a and k_{ij}^b for the cantilever shaft subjected to axial and follower forces are listed, respectively, in Appendix B.

2.3. BOUNDARY FREQUENCY EQUATIONS

By using the linear approximated stiffness influence coefficients, the governing differential equations of a rotational cantilever shaft–disk system subjected to a time-dependent longitudinal load $p(t)$ can be written, in matrix form, as

$$\mathbf{M}\ddot{\mathbf{q}} + \mathbf{G}\dot{\mathbf{q}} + [\mathbf{K}^a + p(t)\mathbf{K}^b]\mathbf{q} = \mathbf{0}, \tag{12}$$

where

$$\mathbf{q} = \{U, \Psi\}^{\mathrm{T}}, \quad \mathbf{M} = \begin{bmatrix} M_D & 0 \\ 0 & I_D \end{bmatrix}, \quad \mathbf{G} = \begin{bmatrix} 0 & 0 \\ 0 & -\mathrm{j}\Omega I_P \end{bmatrix}, \tag{13–15}$$

$$\mathbf{K}^a = \begin{bmatrix} k_{11}^a & k_{12}^a \\ k_{21}^a & k_{22}^a \end{bmatrix}, \quad \mathbf{K}^b = \begin{bmatrix} k_{11}^b & k_{12}^b \\ k_{21}^b & k_{22}^b \end{bmatrix}. \tag{16, 17}$$

For the case in which the shaft–disk system is subjected to a periodic longitudinal load of the form

$$p(t) = p_0 + p_t \cos \theta t, \tag{18}$$

where θ is the longitudinal disturbance frequency. The static and time-dependent components of the load an be expressed as a fraction of the fundamental static buckling load p_{cr} of the non-rotating shaft as

$$p(t) = \alpha_s p_{cr} + \beta_d p_{cr} \cos \theta t, \tag{19}$$

where α_s, and β_d are referred to as the static and dynamic load factor, respectively.

By substitution of equation (19) into equation (12), the governing equations of the system become

$$\mathbf{M}\ddot{\mathbf{q}} + \mathbf{G}\dot{\mathbf{q}} + (\mathbf{K}^a + \alpha_s p_{cr}\mathbf{K}^b + \beta_d p_{cr} \cos \theta t \mathbf{K}^b)\mathbf{q} = \mathbf{0}. \tag{20}$$

Equation (20) represents a system of second order differential equations with periodic coefficients of the Mathieu–Hill type. Application of the theory of linear equations with periodic coefficients, the boundaries between stable and unstable regions can be constructed by periodic solutions of period T and $2T$ [5], where $T = 2\pi/\theta$. In parametric instability problems, the usual interest is to determine the boundaries of the principal instability region in the frequency domain, in which the solutions correspond to the period of $2T$. As a first approximation and focusing only on the case of simple parametric resonance type, the periodic solutions with period $2T$ can be sought in the form

$$\mathbf{q} = \mathbf{a} \sin(\theta t/2) + \mathbf{b} \cos(\theta t/2). \tag{21}$$

By substituting equation (21) into equation (20) and equating the coefficients of the $\sin(\theta t/2)$ and $\cos(\theta t/2)$ terms, a set of linear homogeneous algebraic equations in terms of $\mathbf{a}$ and $\mathbf{b}$ is obtained as

$$\left[\mathbf{K}^a + p_{cr}\left(\alpha_s - \frac{\beta_d}{2}\right)\mathbf{K}^b - \frac{\theta^2}{4}\mathbf{M}\right]\mathbf{a} - \frac{\theta}{2}\mathbf{G}\mathbf{b} = \mathbf{0}, \tag{22}$$

$$\frac{\theta}{2}\mathbf{G}\mathbf{a} + \left[\mathbf{K}^a + p_{cr}\left(\alpha_s + \frac{\beta_d}{2}\right)\mathbf{K}^b - \frac{\theta^2}{4}\mathbf{M}\right]\mathbf{b} = \mathbf{0}. \tag{23}$$

The condition for the set of linear homogeneous equations, equations (22) and (23), to have non-trivial solutions is

$$\begin{vmatrix} \mathbf{K}^a + p_{cr}\left(\alpha_s - \dfrac{\beta_d}{2}\right)\mathbf{K}^b - \dfrac{\theta^2}{4}\mathbf{M}, & -\dfrac{\theta}{2}\mathbf{G} \\ \dfrac{\theta}{2}\mathbf{G}, & \mathbf{K}^a + p_{cr}\left(\alpha_s + \dfrac{\beta_d}{2}\right)\mathbf{K}^b - \dfrac{\theta^2}{4}\mathbf{M} \end{vmatrix} = 0. \tag{24}$$

Equation (24) is referred to as the equation of boundary frequencies and can be used to construct the principal regions of parametric instability. It is worth noting that equation (24) can be further reduced to a quartic equation, therefore the boundaries of unstable regions can be quickly obtained and a lot of computer time is saved.

3. NUMERICAL RESULTS AND DISCUSSION

3.1. ACCURACY OF APPROXIMATE STIFFNESS INFLUENCE COEFFICIENTS

To evaluate the accuracy of the present approximate stiffness influence coefficients, it is convenient to introduce the following non-dimensional parameters:

$$r^2 = \frac{I}{AL^2}, \quad \bar{p} = \frac{pL^2}{EI}, \quad \bar{k}_{11} = \frac{L^3}{EI}k_{11}. \tag{25–27}$$

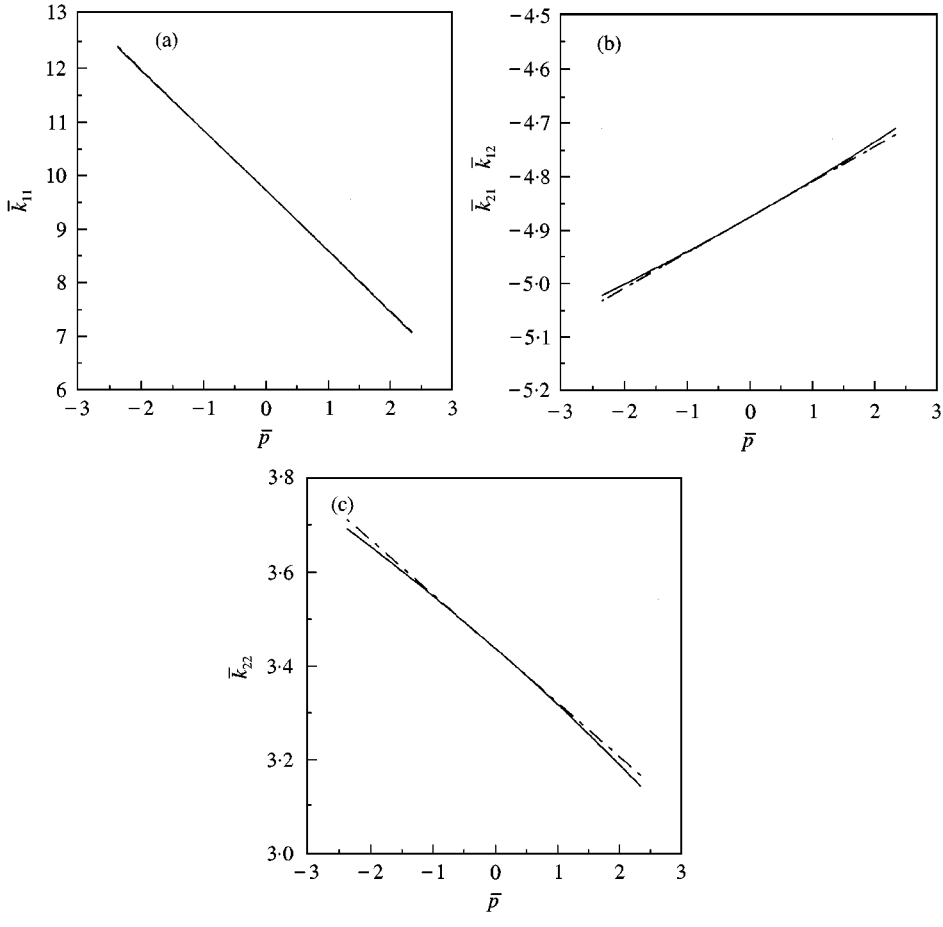

Figure 2. Comparisons of the exact and approximate values of stiffness influence coefficients of a cantilever shaft under axial loading. (a) $\bar{k}_{11}$; (b) $\bar{k}_{12}$ and $\bar{k}_{21}$; and (c) $\bar{k}_{22}$. (— exact; - · - · - linear).

$$\bar{k}_{12} = \frac{L^2}{EI} k_{12}, \quad \bar{k}_{21} = \frac{L^2}{EI} k_{21}, \quad \bar{k}_{22} = \frac{L}{EI} k_{22}. \tag{28–30}$$

Two non-dimensional parameters of the shaft employed here are $r = 0.08$, and $E/\kappa G = 3.0$. The comparisons of the exact and approximate stiffness influence coefficients for the cantilever shafts subjected to an axial loading and a follower loading are given, respectively, in Figures 2 and 3. The magnitude of the non-dimensional longitudinal load in Figures 2 and 3 is considered to be within the interval $(-\bar{p}_{cr}, +\bar{p}_{cr})$, where $\bar{p}_{cr}$ is the non-dimensional critical load of the corresponding system ($\bar{p}_{cr} = 2.3558$ for the case of cantilever shaft subjected to an axial loading, and $\bar{p}_{cr} = 12.3019$ for the case of cantilever shaft subjected to a follower loading). As can be seen from Figures 2 and 3, the present approximate values of $\bar{k}_{ij}$ except for $\bar{k}_{21}$ and $\bar{k}_{22}$ in Figure 3 are very close to their exact values over a considerable range of the longitudinal load. Fortunately, only the element $\bar{k}_{11}$ is the dominant parameter in the present study, so the error induced by the discrepancies between approximate and exact values of $\bar{k}_{21}$ and $\bar{k}_{22}$ is limited.

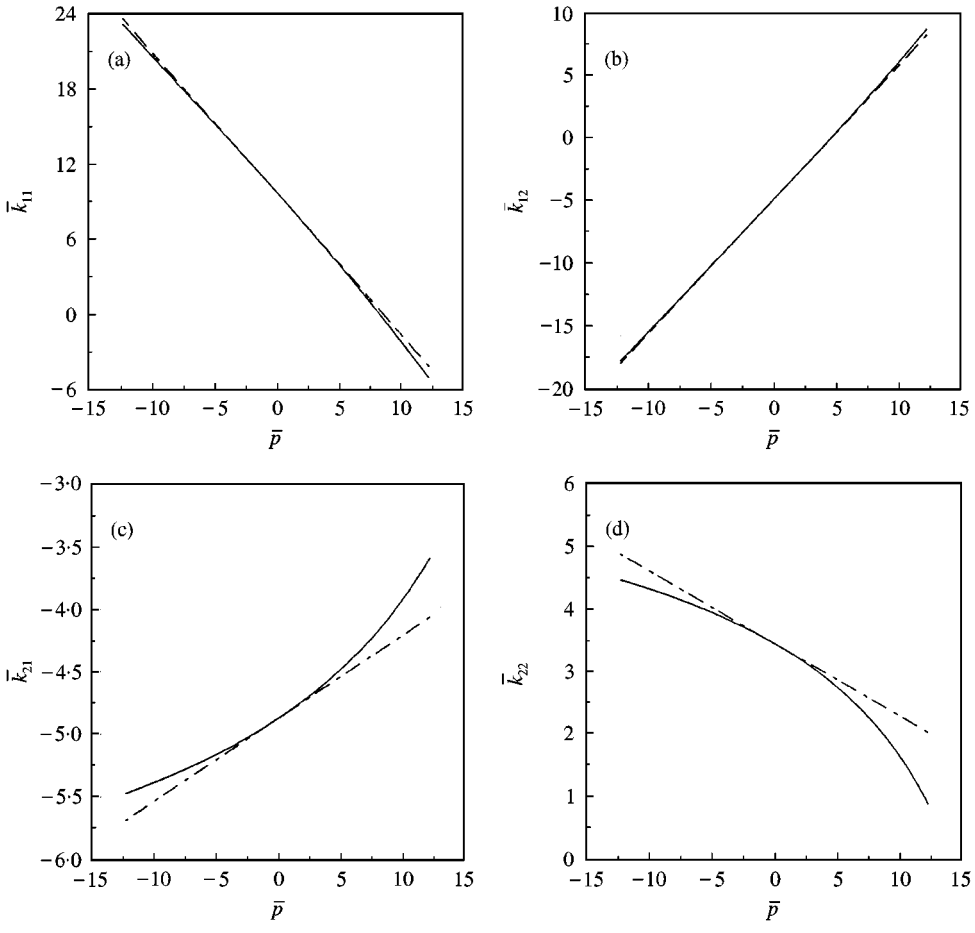

Figure 3. Comparisons of the exact and approximate stiffness influence coefficients of a cantilever shaft under follower loading. (a) $\bar{k}_{11}$; (b) $\bar{k}_{12}$; (c) $\bar{k}_{21}$; and (d) $\bar{k}_{22}$. (— exact; - - - - linear).

3.2. INSTABILITY REGIONS

To evaluate the accuracy of the present lumped mass model, the basic parameters of the system, as listed in Table 1, are the same as used by Chen and Ku [4]. The regions of parametric instability obtained, respectively, by the present lumped mass model and finite element method with the static load factor $\alpha_s = 0.5$ are shown and compared in Figure 4, in which the unstable regions are shaded in these and the following diagrams. It is observed that the agreement of the principal (first) unstable regions obtained by the present lumped mass model with those by the finite element method [4] is good. Because the inertia of the shaft is neglected in the present model, the unstable regions, as compared with the results of reference [4], are slightly shifted right in parallel to the dynamic load factor axis. Admittedly, a less-good agreement in the second unstable regions is detected. This is because that the mass ratio of disk to shaft is only 1.16. For neglecting 46% mass of the system, however, the boundary frequencies of the second unstable regions obtained by the present model are only 15% higher than that by the finite element method. If the mass ratio of disk to shaft exceeds 3.0, a satisfactory accuracy of the present model can be expected. In addition, the matrix dimension accessed in the finite element method for an accepted

TABLE 1

Configuration data and material properties of the cantilever shaft–disk system used in reference [4]

$L = 50.0$ cm (length of the shaft)	$\phi = 2.0$ cm (diameter of the shaft)
$E = 207.0$ GPa (Young's modulus of the shaft)	$G = 79.6$ GPa (shear modulus of the shaft)
$\rho = 7680.0$ kg/m^3 (density of the shaft)	$\kappa = 0.89$ (shear coefficient of the shaft)
$M_D = 1.401$ kg (mass of the disk)	$I_D = 0.0136$ kg-m^2 (diameter mass moment of inertia of the disk)
$I_P = 0.0272$ kg-m^2 (polar mass moment of inertia of the disk)	$\omega_n = 159.805$ rad/s (natural frequency of the non-rotating shaft–disk system)
$p_{cr} = 16.0$ kN (static buckling load of the shaft)	

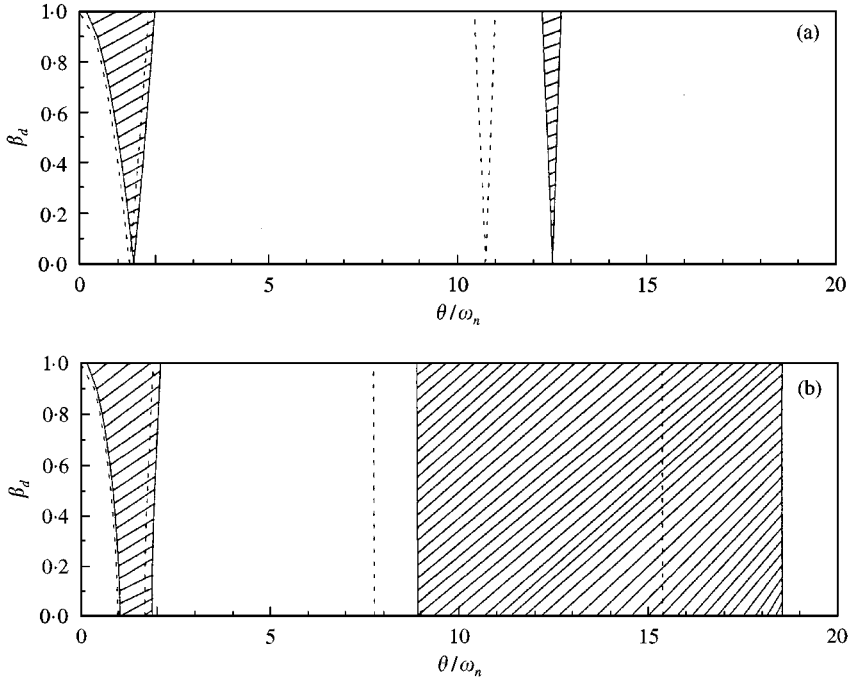

Figure 4. Comparison of the unstable regions obtained by two different models with the static load factor $\alpha_s = 0{\cdot}5$. (a) $\Omega = 0$ and (b) $\Omega = 1000$ r.p.m. (—, present; - - -, finite element model).

accuracy needs 80×80 after the governing equation of the system is written in the first order state vector form. However, the boundaries of the unstable regions are obtained just by solving a quartic equation in the present model, therefore a lot of computer time can be saved.

To simplify subsequent discussion, the following non-dimensional inertial quantities of the disk, rotational speed and whirl speed are introduced.

$$\bar{M}_D = \frac{M_D}{\rho AL}, \quad \bar{I}_D = \frac{I_D}{\rho AL^3}, \quad \bar{I}_P = \frac{I_P}{\rho AL^3}, \quad \bar{\Omega}^2 = \frac{\rho AL^4\Omega^2}{EI}, \quad \bar{\omega}^2 = \frac{\rho AL^4\omega^2}{EI}, \quad (31\text{–}35)$$

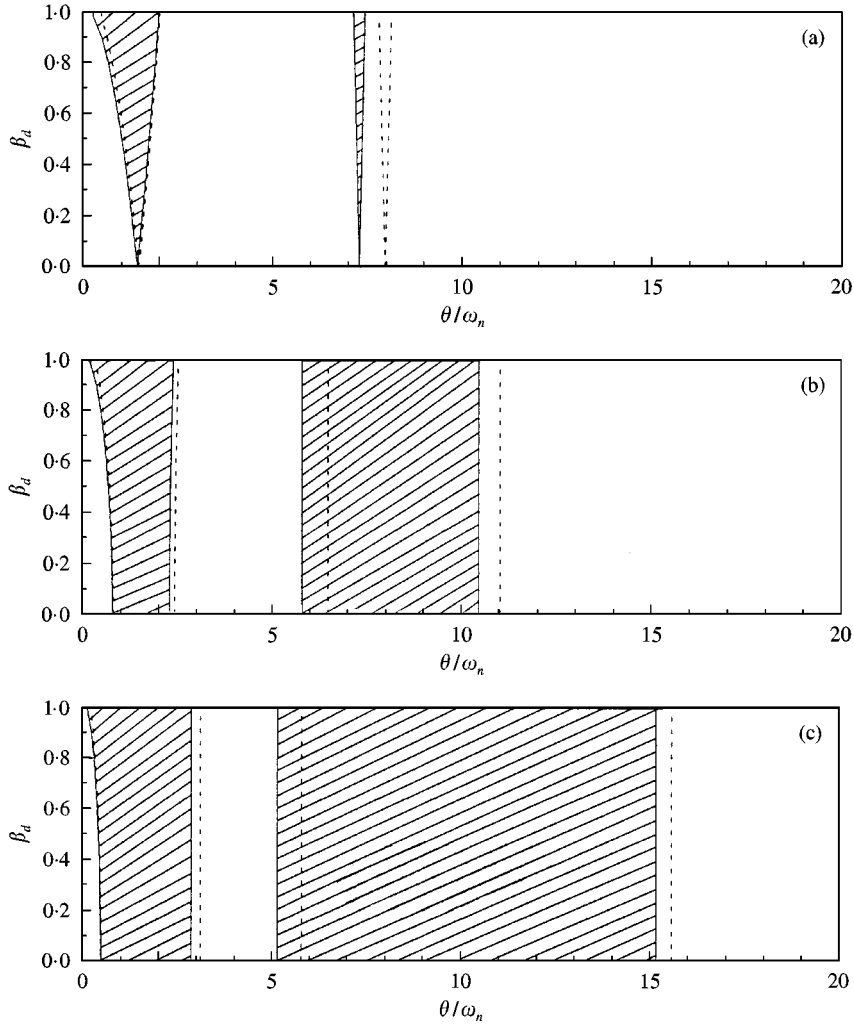

Figure 5. Effect of shear deformation on the unstable regions of the cantilever shaft–disk system subjected to the axial-type loading with $\alpha_s = 0{\cdot}5$, (a) $\bar{\Omega} = 0$; (b) $\bar{\Omega} = 1$; (c) $\bar{\Omega} = 2$. (—, Timoshenko beam theory; - - -, Euler–Bernoulli beam theory).

where ρ is the density of the shaft. For typical numerical simulations of the system, the basic non-dimensional data $r = 0.08$, $E/\kappa G = 3.0$, $\bar{M}_D = 5.0$, $\bar{I}_D = 0.8$, and $\bar{I}_P = 1.6$ are used.

The effect of shear deformation (i.e., the difference between Euler–Bernoulli beam theory and Timoshenko beam theory) on the unstable regions of a cantilever shaft–disk subjected to an axial-type loading with three different rotational speeds is shown in Figure 5, where ω_n is the fundamental natural frequency of the non-rotating cantilever shaft–disk system obtained by Timoshenko beam theory. Figure 5 shows that the unstable regions obtained by Euler–Bernoulli beam theory are shifted away from the dynamic load factor axis as compared to that by Timoshenko beam theory. Therefore, neglecting shear deformation in the analysis of the parametric instability is not on the side of safety. In other words, shear deformation has a destabilizing effect on the parametric instability of the present system. Another observation from Figure 5 shows that as the rotational speed increases, the boundaries of the unstable regions are shifted outwardly, and the widths of these unstable

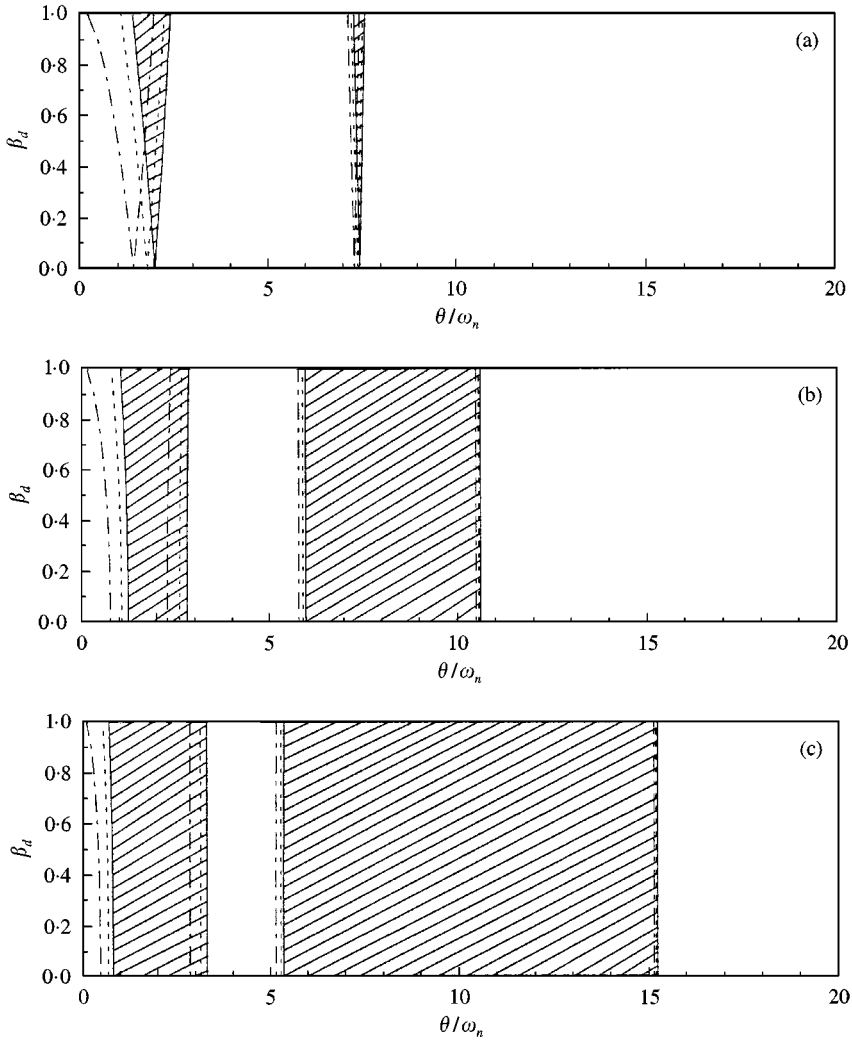

Figure 6. Effect of the static load factor α_s on the unstable regions of the cantilever shaft–disk system subjected to the axial-type loading. (a) $\bar{\Omega} = 0$; (b) $\bar{\Omega} = 1$; (c) $\bar{\Omega} = 2$. (—, $\alpha_s = 0{\cdot}0$; - - -, $\alpha_s = 0{\cdot}2$; - · - · -, $\alpha_s = 0{\cdot}5$).

regions are drastically increased; therefore, the system becomes more prone instability. Since the gyroscopic moment is proportional to the rotational speed, it leads to a conclusion that the gyroscopic moment has a destabilizing effect on the parametric instability problem. The numerical results also show that the left unstable boundary is constructed by the backward precessional mode, whereas the right unstable boundary is constructed by the forward precessional mode.

The effect of the static load factor α_s on the unstable regions for different rotational speeds is studied next. The results are shown in Figure 6 for the axial-type loading and in Figure 7 for the follower-type loading. Here the static load factor α_s is taken as 0, 0.2 and 0.5, respectively. It is seen from Figure 6 that if a higher value of α_s is applied, the unstable regions are shifted left closer to the dynamic load axis; thus the system is more unstable because the system will have parametric resonance occurring at the lower axial disturbance frequencies. In contrast to the case of periodic axial loading, as α_s increased, the first

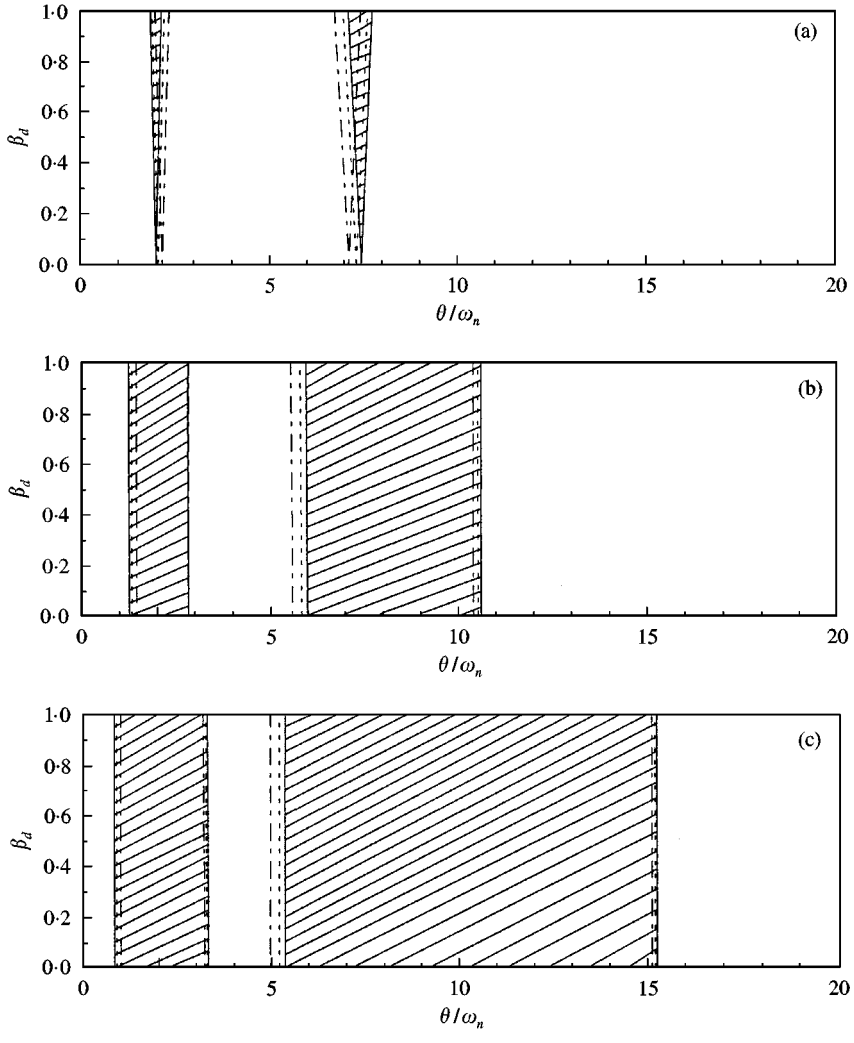

Figure 7. Effect of the static load factor α_s on the unstable regions of the cantilever shaft–disk system subjected to the follower-type loading. (a) $\bar{\Omega} = 0$; (b) $\bar{\Omega} = 1$; (c) $\bar{\Omega} = 2$. (—, $\alpha_s = 0{\cdot}0$; - - -, $\alpha_s = 0{\cdot}2$; - · - · -, $\alpha_s = 0{\cdot}5$).

unstable region caused by the periodic follower loading is shifted right away from the dynamic load axis for $\bar{\Omega} = 0$, but shifted inwardly, and the width of the first unstable region is slightly decreased for $\bar{\Omega} = 1$ and 2. The different effects of the periodic axial loading and the periodic follower loading can be realized by the load–frequency curves as shown in Figure 8. The rotational speeds $\bar{\Omega}$ of the system considered here are, respectively, 0 for Figure 8(a) and 2 for Figure 8(b). In Figure 8, the positive whirl speed indicates the forward precession, while the negative whirl speed denotes the backward precession. For the case of $\bar{\Omega} = 0$, of course, there is no distinction between forward and backward precessions. The magnitudes of the positive natural frequencies should be equal to those of the corresponding negative natural frequencies. In Figure 8(a), the system is reduced to a non-rotating structure problem and all curves are symmetric about the horizontal line of $\bar{\omega} = 0$. As observed in Figure 8(a), both the first and second natural frequencies decrease with the increasing of axial loading, while the first natural frequency increases as the follower loading increased. Although the behavior of the boundary frequencies of the

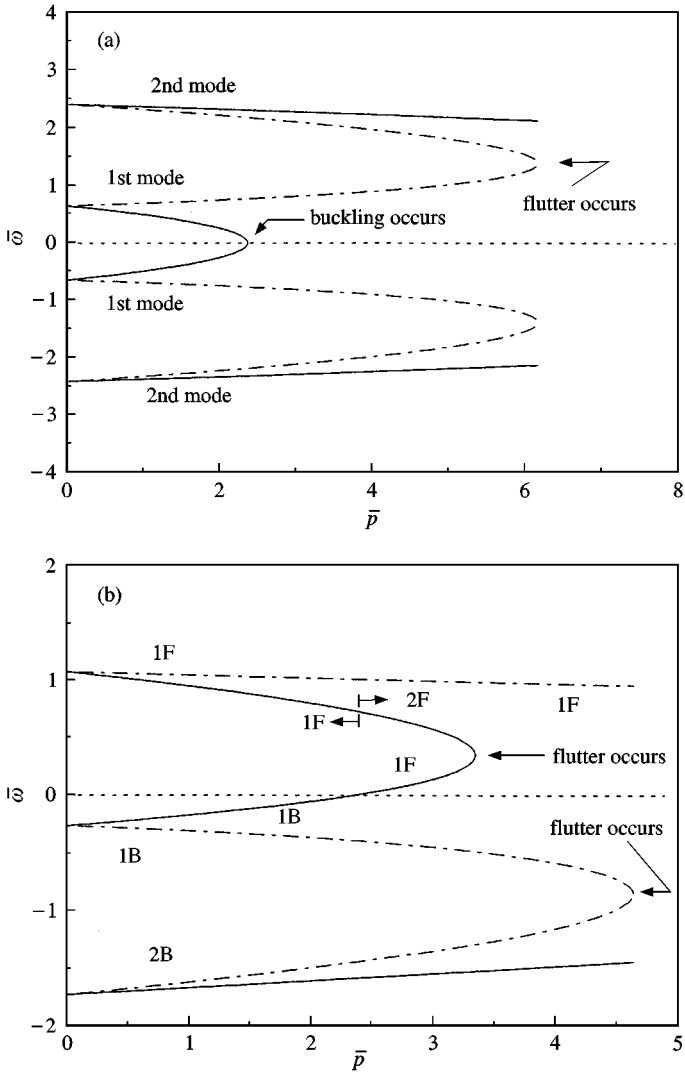

Figure 8. The load–frequency curves of the cantilever shaft–disk system ($\bar{M}_D = 5{\cdot}0, \bar{I}_D = 0{\cdot}8, \bar{I}_P = 1{\cdot}6$). (a) $\bar{\Omega} = 0$; (b) $\bar{\Omega} = 2$. (—, axial force; - - -, follower force).

unstable regions is not identical to that of natural frequencies, their characteristics are essentially similar. According to these load–frequency curves, the difference between Figures 6(a) and 7(a) an be clearly realized. In Figure 8(b), the curves are not symmetric due to the presence of the gyroscopic moment. Both the first forward whirl speed (1F) and the first backward whirl speed (1B) decrease with the increasing axial loading before the non-dimensional axial loading exceeds the static buckling load, $\bar{p}_{cr}$ ($= 2.3558$), of the corresponding non-rotating cantilever beam. This is the reason why the first unstable regions in Figures 6(b) and 6(c) are shifted left to the dynamic load factor axis when the larger static load factor α_s is applied. On the other hand, the whirl speed of the first forward mode (1F) increases and that of the first backward mode (1B) decreases with the increasing follower force. Consequently, the characteristics of the first unstable regions in Figure 7(b) and 7(c) can be expected.

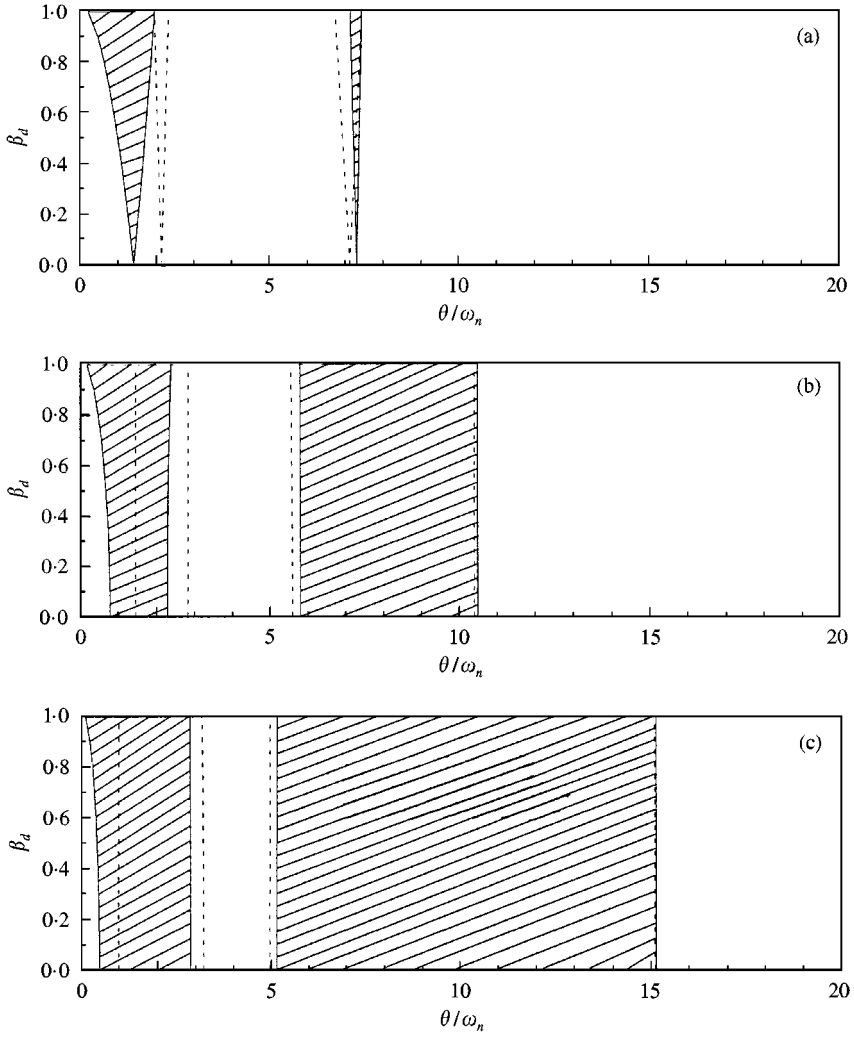

Figure 9. Effect of the loading type on the unstable regions of the cantilever shaft–disk system with $\alpha_s = 0{\cdot}5$. (a) $\bar{\Omega} = 0$; (b) $\bar{\Omega} = 1$; (c) $\bar{\Omega} = 2$. (—, axial force; - - -, follower force).

Finally, the effect of the loading type on the unstable regions of the cantilever shaft–disk system is compared in a clearer manner and the result are shown in Figure 9. From the properties of the load–frequency curves, as indicated in Figure 8, the first unstable region caused by the periodic follower force is in the right side to that by the periodic axial force. Therefore, under the same static load factor, a periodic axial loading makes the system more unstable than a periodic follower force does.

4. CONCLUSIONS

A lumped mass model is proposed to determine the regions of parametric instability of a cantilever shaft–disk system subjected to periodic longitudinal forces. By the use of Bolotin's method, the equation of boundary frequencies can be obtained and is used to

determine the boundaries between stable and unstable regions. As compared to the unstable regions obtained from the finite element method, the present results show not only good agreement with them but also much easier to construct the unstable regions. From the results of numerical simulations, the following conclusions can be drawn.

(a) For each unstable region, the left-side boundary is constructed by the backward precessional mode, whereas the right-side boundary is constructed by the forward precessional mode.
(b) Both shear deformation and gyroscopic moment have a destabilizing effect on the parametric instability of the present cantilever shaft–disk system.
(c) The system will have parametric resonance occurring at lower axial disturbance frequency if a higher value of static load factor is applied.
(d) If a higher value of static load factor is applied, the first unstable region caused by periodic follower force is shifted inwardly, and the width is slightly decreased.
(e) The periodic axial loading makes the rotor system more unstable than the periodic follower force does under the same static load factor.

REFERENCES

1. T. YAMAMOTO, H. OTA and K. KONO 1968 *ASME Journal of Applied Mechanics* **35**, 313–321. On the unstable vibrations of a shaft with unsymmetrical stiffness carrying an unsymmetrical rotor.
2. A. UNGER and M. A. BRULL 1981 *ASME Journal of Applied Mechanics* **48**, 948–958. Parametric instability of a rotating shaft due to pulsating torque.
3. S. K. SINHA 1989 *AIAA Journal* **27**, 1653–1655. Stability of a viscoelastic rotor–disk system under dynamic axial loads.
4. L. W. CHEN and D. M. KU 1992 ASME *Journal of Vibration and Acoustics* **114**, 326–329. Dynamic stability of a cantilever shaft–disk system.
5. V. V. BOLOTIN 1964 *The Dynamic Stability of Elastic Systems*. Holden-Day, San Francisco.
6. T. IWATSUBO, M. SAIGO and Y. SUGIYAMA 1973 *Journal of Sound and Vibration* **30**, 65–77. Parametric instability of clamped–clamped and clamped–simply supported columns under periodic axial load.
7. J. THOMAS and B. A. H. ABBAS 1976 *ASME Journal of Engineering for Industry* **98**, 1145–1151. Dynamic stability of Timoshenko beams by finite element method.
8. H. ZIEGLER 1977 *Principles of Structural Stability*. Basel, Stuttgart: Birkhäuser.
9. B. P. SHASTRY and G. V. RAO 1984 *Computers and Structures* **19**, 823–827. Dynamic stability of bars considering shear deformation and rotatory inertia.
10. J. W. LUND 1974 *ASME Journal of Engineering for Industry* **96**, 509–517. Stability and damped critical speeds of a flexible rotor in fluid-film bearings.
11. B. T. MURPHY and J. M. VANCE 1983 *ASME Journal of Engineering for Power* **105**, 591–595. An improved method for calculating critical speeds and rotordynamic stability of turbomachinery.
12. K. E. ROUCH and J. S. KAO 1979 *Journal of Sound and Vibration* **66**, 119–140. A taped beam finite element for rotor dynamics analysis.
13. H. D. NELSON 1980 *ASME Journal of Mechanical Design* **102**, 793–803. A finite rotating shaft element using Timoshenko beam theory.
14. R. L. ESHLEMAN and R. A. EUBANKS 1969 *ASME Journal of Engineering for Industry* **91**, 1180–1188. On the critical speeds of a continuous rotor.
15. J. WAUER 1982 *International Journal of Solids and Structures* **18**, 459–466. On the stability of rotating, axially loaded, homogeneous shafts.
16. J. W. Z. ZU and R. P. S. HAN 1992 ASME *Journal of Applied Mechanics* **59**, S197–S204. Natural frequencies and normal modes of a spinning Timoshenko beam with general boundary conditions.
17. L. W. CHEN and H. C. SHEU 1997 *Journal of Sound and Vibration* 200, 41–61. The stability behavior of a non-conservative spinning Timoshenko shaft with an overhung disk.
18. V. RAMAMURTI and A. R. PRADEEP SIMA 1987 *Journal of Sound and Vibration* **117**, 578–582. Finite element calculation of critical speeds of rotation of shafts with gyroscopic action of discs.

19. A. D. DIMAROGONAS and S. HADDA 1992 *Vibration for Engineers*. Prentice-Hall, Englewood Cliffs, NJ.
20. K. CZOLCZYNSKI and K. P. MARYNOWSKI 1992 *Journal of Sound and Vibration* **154**, 281–288. Instabilities of the elastically supported Laval rotor subjected to a longitudinal force.

APPENDIX A. STIFFNESS INFLUENCE COEFFICIENTS OF CANTILEVER SHAFTS SUBJECTED TO LONGITUDINAL FORCES

Figure A1 shows a cantilever shaft subjected to a longitudinal load at free end. In order to obtain the stiffness influence coefficients of the cantilever shaft, it is convenient to start with the flexibility influence coefficients rather than stiffness influence coefficients at this stage. To this end, a transverse loading F_y and a moment M_z are applied at the free end of the shaft. The governing differential equations and corresponding boundary conditions for such an elastic system can be easily achieved by use of the principle of virtual work

$$\delta \Pi - \delta W_{NC} = 0, \tag{A1}$$

where Π is the potential energy of the system, and δW_{NC} is the vitual work done by non-conservative external load.

Taking into account the shear deformation, the potential energy Π for a cantilever shaft of cross-sectional area A and moment of inertia of the shaft cross-section I is given by

$$\Pi = \int_0^L \left[\frac{EI}{2} \left(\frac{\mathrm{d}\gamma}{\mathrm{d}x} \right)^2 + \frac{\kappa GA}{2} \left(\frac{\mathrm{d}v}{\mathrm{d}x} - \gamma \right)^2 - \frac{1}{2} p \left(\frac{\mathrm{d}v}{\mathrm{d}x} \right)^2 \right] \mathrm{d}x - F_y v(L) + M_z \gamma(L), \tag{A2}$$

where E, G and κ are the Young's modulus, shear modulus and shear coefficient of the shaft, respectively, v and w are the translations in the y- and z-directions, and β and γ are the small rotations about y- and z-axis.

The only virtual work included in this study is due to the longitudinal load p and can be expressed as

$$\delta W_{NC} = -\mu p \gamma(L) \delta v(L), \tag{A3}$$

where $\mu = 0$ implies that the load is a conservative force acting in the axial direction of the undeformed shaft and then $\delta W_{NC} = 0$, and $\mu = 1$ implies that the load is a fully tangential follower force.

Upon substituting equations (A2) and (A3) into the principle of virtual work, equation (A1), the governing differential equations for the shaft are obtained and shown in the following way:

$$EI \frac{\mathrm{d}^2 \gamma}{\mathrm{d}x^2} + \kappa GA \left(\frac{\mathrm{d}v}{\mathrm{d}x} - \gamma \right) = 0, \tag{A4}$$

$$(\kappa GA - p) \frac{\mathrm{d}^2 v}{\mathrm{d}x^2} - \kappa GA \frac{\mathrm{d}\gamma}{\mathrm{d}x} = 0. \tag{A5}$$

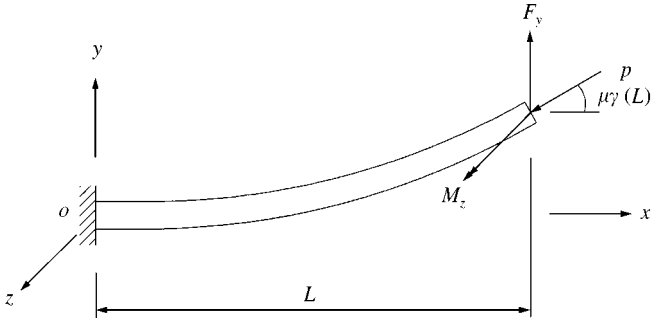

Figure A1. A longitudinally loaded cantilever shaft with transverse loading and moment applied at its free end.

The necessary and sufficient boundary conditions are:
(a) Clamped end (at $x = 0$):

$$v = 0, \qquad \gamma = 0. \tag{A6, A7}$$

(b) Free end (at $x = L$):

$$EI\frac{\mathrm{d}\gamma}{\mathrm{d}x} = M_z, \qquad (\kappa GA - p)\frac{\mathrm{d}v}{\mathrm{d}x} - (\kappa GA - \mu p)\gamma - F_y = 0. \tag{A8, A9}$$

By applying the Laplace transformation with respect to x, the deflection and rotation at $x = L$ can be obtained and expressed, in matrix form, as

$$\begin{Bmatrix} v(L) \\ \gamma(L) \end{Bmatrix} = \begin{bmatrix} c_{11} & c_{12} \\ c_{21} & c_{22} \end{bmatrix} \begin{Bmatrix} F_y \\ M_z \end{Bmatrix}, \tag{A10}$$

where c_{ij}, $i, j = 1, 2$, are flexibility influence coefficients of the cantilever shaft, and can be expressed as follows:
(a) The cantilever shaft subjected to an axial load

$$c_{11} = \begin{cases} -\dfrac{L}{p} + \dfrac{kEI\sin(kL)}{p^2\cos(kL)}, & \text{when } p > 0 \text{ (compression)}, \\ -\dfrac{L}{p} - \dfrac{kEI\sinh(kL)}{p^2\cosh(kL)}, & \text{when } p < 0 \text{ (tension)}, \end{cases} \tag{A11}$$

$$c_{12} = \begin{cases} \dfrac{1 - \cos(kL)}{p\cos(kL)}, & \text{when } p > 0 \text{ (compression)}, \\ \dfrac{1 - \cosh(kL)}{p\cosh(kL)}, & \text{when } p < 0 \text{ (tension)}, \end{cases} \tag{A12}$$

$$c_{21} = c_{12}, \tag{A13}$$

$$c_{22} = \begin{cases} \dfrac{\sin(kL)}{KEI\cos(kL)}, & \text{when } p > 0 \text{ (compression)}, \\ \dfrac{\sinh(kL)}{KEI\cosh(kL)}, & \text{when } p < 0 \text{ (tension)}, \end{cases} \tag{A14}$$

where

$$k = \left[\frac{\kappa GA|p|}{EI(\kappa GA - p)}\right]^{1/2}. \tag{A15}$$

(b) The cantilever shaft subjected to a follower load;

$$c_{11} = \begin{cases} \dfrac{KEI\sin(kL)}{p^2} - \dfrac{L\cos(kL)}{p}, & \text{when } p > 0 \text{ (compression)}, \\ -\dfrac{KEI\sinh(kL)}{p^2} - \dfrac{L\cosh(kL)}{p}, & \text{when } p < 0 \text{ (tension)}, \end{cases} \tag{A16}$$

$$c_{12} = \begin{cases} -\dfrac{1}{p} + \dfrac{\cos(kL)}{p} + \dfrac{kL(\kappa GA - p)\sin(kL)}{p\kappa GA}, & \text{when } p > 0 \text{ (compression)}, \\ -\dfrac{1}{p} + \dfrac{\cosh(kL)}{p} - \dfrac{kL(\kappa GA - p)\sinh(kL)}{p\kappa GA}, & \text{when } p < 0 \text{ (tension)}, \end{cases} \tag{A17}$$

$$c_{21} = \begin{cases} \dfrac{1 - \cos(kL)}{p} & \text{when } p > 0 \text{ (compression)}, \\ \dfrac{1 - \cosh(kL)}{p} & \text{when } p < 0 \text{ (tension)}, \end{cases} \tag{A18}$$

$$c_{22} = \begin{cases} \dfrac{k(\kappa GA - p)\sin(kL)}{p\kappa GA}, & \text{when } p > 0 \text{ (compression)}, \\ -\dfrac{k(\kappa GA - p)\sinh(kL)}{p\kappa GA} & \text{when } p < 0 \text{ (tension)}, \end{cases} \tag{A19}$$

From the relation between stiffness and flexibility influence coefficients, equation (A10) can be rewritten as

$$\begin{Bmatrix} F_y \\ M_z \end{Bmatrix} = \begin{bmatrix} k_{11} & k_{12} \\ k_{21} & k_{22} \end{bmatrix} \begin{Bmatrix} v(L) \\ \gamma(L) \end{Bmatrix}, \tag{A20}$$

where

$$k_{11} = \frac{c_{22}}{\Delta}, k_{12} = \frac{c_{12}}{\Delta}, \quad k_{21} = \frac{c_{21}}{\Delta}, k_{22} = \frac{c_{11}}{\Delta}, \Delta = c_{11}c_{22} - c_{12}c_{21}. \tag{A21–A25}$$

By using the co-ordinate transformation or the same procedure as above, the relation between displacement vector and force vector in xz plane can be easily obtained as

$$\begin{Bmatrix} F_z \\ M_y \end{Bmatrix} = \begin{bmatrix} k_{11} & -k_{12} \\ -k_{21} & k_{22} \end{bmatrix} \begin{Bmatrix} w(L) \\ \beta(L) \end{Bmatrix}. \tag{A26}$$

APPENDIX B. k_{ij}^a AND k_{ij}^b COEFFICIENTS FOR CANTILEVER SHAFTS

(a) The cantilever shaft subjected to an axial load:

$$k_{11}^a = 12EI/\lfloor L^3(1 + 12\Phi\rfloor, \quad k_{11}^b = -6(1 + 20\Phi + 120\Phi^2)/\lfloor 5L(1 + 12\Phi)^2\rfloor, \quad \text{(B1, B2)}$$

$$k_{12}^a = -6EI\lfloor L^2(1 + 12\Phi)\rfloor, \quad k_{12}^b = 1/\lfloor 10L(1 + 12\Phi)^2\rfloor, \quad \text{(B3, B4)}$$

$$k_{21}^a = k_{12}^a, \quad k_{21}^b = k_{12}^b, \quad \text{(B5, B6)}$$

$$k_{22}^a = 4EI(1 + 3\Phi)/\lfloor L^2(1 + 12\Phi)\rfloor, \quad k_{22}^b = -2L(1 + 15\Phi + 90\Phi^2)/\lfloor 15(1 + 12\Phi)^2\rfloor, \quad \text{(B7, B8)}$$

where $\Phi = EI/\kappa GAL^2$.

It is noteworthy that if the parameter Φ is omitted, then the above factors correspond to the conventional Euler–Bernoulli beam model.

(b) The cantilever shaft subjected to a follower load: All factors are the same as the case (a) except for

$$k_{12}^b = (11 + 240\Phi + 1440\Phi^2)/\lfloor 10L(1 + 12\Phi^2\rfloor. \quad \text{(B9)}$$

The stiffness matrix in this case is asymetric due to $k_{12}^b \neq k_{21}^b$. This result can be expected because the follower force is a non-conservative load.